Weber, M., Wicks, C., Le Stunff, Y., Romanowicz, B., Kruger, F. (2015): Seismic evidence for a steeply dipping reflector--stagnant slab in the mantle transition zone. - *Geophysical Journal International*, *200*, 2, p. 1235-1251.

DOI: http://doi.org/10.1093/gji/ggu438

Geophysical Journal International

Geophys. J. Int. (2015) **200,** 1235–1251
GJI Seismology

doi: 10.1093/gji/ggu438

Seismic evidence for a steeply dipping reflector—stagnant slab in the mantle transition zone

Michael Weber,[1,*,†] Charles Wicks Jr.,[1,‡] Yves Le Stunff,[2,§] Barbara Romanowicz[2,3] and Frank Krüger[4]

[1] *Institute for Geophysics, University of Göttingen, Germany. E-mail: michael.weber@gfz-potsdam.de*
[2] *Seismological Laboratory and Department of Geology and Geophysics, University of California, Berkeley, CA* 94720, *USA*
[3] *College de France, Paris, France*
[4] *Institute of Earth and Environmental Science, University of Potsdam, Potsdam, Germany*

Accepted 2014 November 10. Received 2014 October 23; in original form 2014 January 7

SUMMARY

Studies of seismic tomography have been highly successful at imaging the deep structure of subduction zones. In a study complementary to these tomographic studies, we use array seismology and reflected waves to image a stagnant slab in the mantle transition zone. Using *P* and *S* (SH) waves we find a steeply dipping reflector centred at *ca*. 400 km depth and *ca*. 550 km west of the present Mariana subduction zone (at 20N, 140E). The discovery of this anomaly in tomography and independently in array seismology (this paper) helps in understanding the evolution of the Mariana margin. The reflector/stagnant slab may be the remains of the hypothetical North New Guinea Plate, which was theorized to have subducted *ca*. 50 Ma.

Key words: Mantle processes; Composition of the mantle; Seismic tomography; Wave scattering and diffraction; Subduction zone processes; Volcanic arc processes; Continental margins: convergent; Pacific Ocean.

1 INTRODUCTION

Imaging the deep structure of subduction zones has long been a central topic of geosciences and especially of seismology (see e.g. van der Hilst *et al.* 1991, 1997; Fukao *et al.* 1992; Grand *et al.* 1997; Stern 2002).

In the last 15 yr, improvements in resolution of global and regional tomographic models have further clarified the diversity of behaviours of subducted slabs in the upper mantle transition zone (MTZ). *P*-wave tomographic models with high resolution around subduction zones have shown that some slabs, such as in middle-America, clearly penetrating into the lower mantle, while others appear to stagnate in the transition zone (Karason & van der Hilst 2000; Grand 2002; Li *et al.* 2008; Obayashi *et al.* 2009, 2013; Simmons *et al.* 2012). A more recent *P* tomographic study indicates that some slabs may also stagnate deeper, around 900–1000 km depth (Fukao & Obayashi 2013). While global shear wave tomographic models do not yet attain the same level of resolution in subduction zones, they also indicate a broad zone of fast velocity anomalies in the transition zone (e.g. at 600 km depth) associated with slabs around the Pacific rim, whereas this zone is much narrower and present only in some subduction zones at depths of 1000 km (e.g. Kustowski *et al.* 2008; Panning *et al.* 2010; Ritsema *et al.* 2011).

At the same time, using array analysis of various precursors or post-cursors to major compressive phases such as P, PP and PKP, a number of studies have reported evidence for the presence of strong scatterers in the transition zone (e.g. Kaneshima & Helffrich 2003), in the mid-mantle (Kaneshima & Helffrich 1999, 2009; Kaneshima 2003; Niu *et al.* 2003; Vanacore *et al.* 2006; Rost *et al.* 2008), or near the base of the mantle (Cao & Romanowicz 2007). These scatterers have been associated with dipping interfaces that may represent the borders of chunks of remnant slab material distributed throughout the mantle. The strong scattering observed indicates that the nature of the corresponding heterogeneity cannot be only thermal, but must comprise a compositional component.

Some 19 yr ago, that is before most of these studies, the authors (Wicks *et al.* 1995, 1996, 1997; Wicks & Weber 1996) first presented evidence for the presence of a reflector/stranded slab in the MTZ near the Mariana subduction zone, using array analysis techniques applied to the observations of a large earthquake in the Marianas on a medium size array in California. Unfortunately, at that time (1995–1998), we were not able to publish our findings, due to competing interests and lack of independent observations supporting our conclusions. Fortunately, this has changed now with

*Now at: GFZ Potsdam, Telegrafenberg E325, D-14473 Potsdam, Germany.
†Now at: University of Potsdam, Potsdam, Germany.
‡Now at: USGS, 345 Middlefield Rd MS 977, Menlo Park, CA 94025, USA.
§Now at: TOTAL E&P, 2, place Jean Millier – la Défense 6, F-92078 Paris, La Défense Cedex, France.

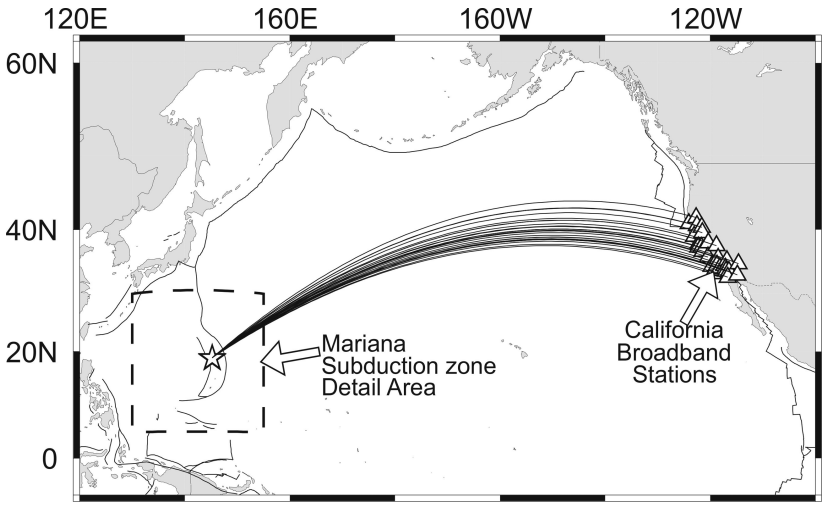

Figure 1. Regional source–receiver location map. The detailed study area (Fig. 2) and great circle paths from Mariana events to California broad-band stations are shown.

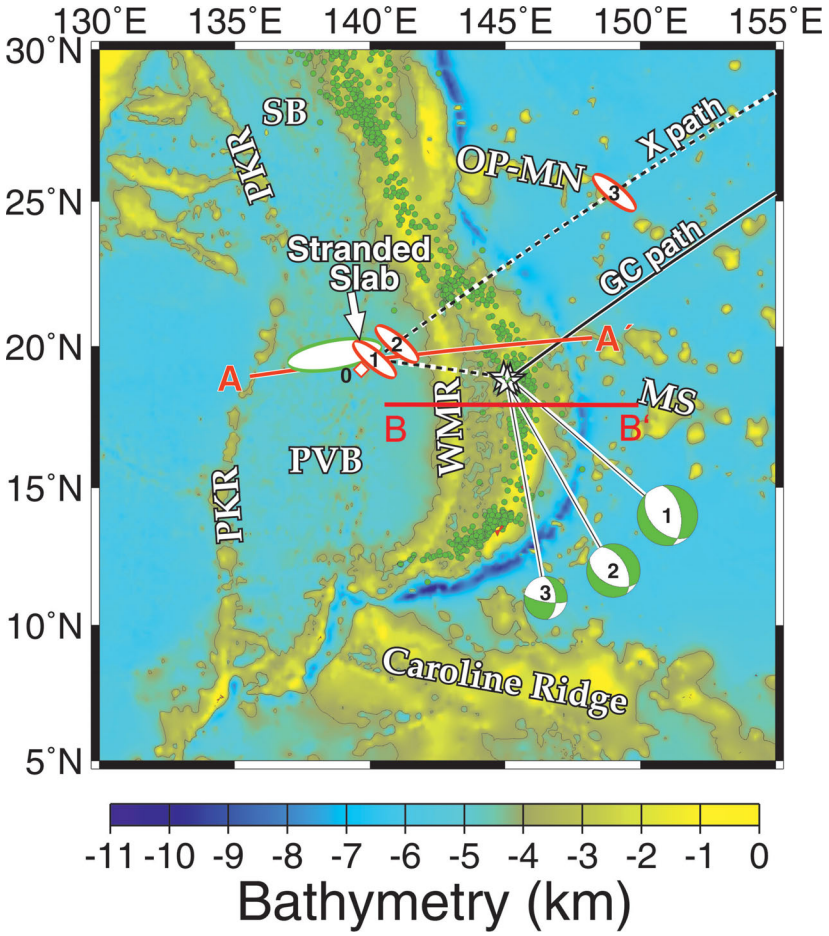

Figure 2. Detailed study area map. Ocean depth is indicated with the colour scale. The single depth contour is at 4 km depth. The bathymetry data comes from the National Geophysical Data Centre archive. Prominent subsea features are labelled with the following abbreviations: Magellan Seamounts 'MS', Ogasawara Plateau-Markus Neker Ridge 'OP-MN', Palau Kyushu Ridge 'PKR', Parece Vela Basin 'PVB', Shikoku Basin 'SB' and the West Mariana Ridge 'WMR'. Green circles are epicentres of earthquakes deeper than 100 km from the Global Hypocentre Data Base of the United States Geological Survey and National Earthquake Information Centre (NEIC). The labelled focal mechanisms, derived from Harvard central moment tensor (CMT) solutions, correspond to Events 1–3, the earthquakes used in this study (Table 1). The projection of the ray path of *P* from Event 1 to station PKD1 in California is the great circle path labelled 'GC path'. The red line labelled A on the west and A′ on the east end marks the location of the cross-section shown in Figs 12 and 13. The profile B–B′ shows the location of the cross section given in Figs 16 and 17. The white diamond and ellipses labelled '0, 1, 2, 3', respectively, correspond to possible reflected/converted phases shown schematically in Fig. 8. The green ellipse encloses the jackknife realizations for Event 2, for details see text. Only location '1' fits all observations.

Table 1. Earthquake information from USGS/HRVD CMT catalogue—events in 1995.

Event	Origin (yr/m/d:hr:mn:s)	Lat (°)	Lon (°)	Depth (km)	M_w
1	1995/08/23:07:06:04	18.82N	145.30E	600	7.0
2	1995/08/24:01:55:36	18.89N	145.15E	591	6.2
3	1995/08/25:11:29:40	18.71N	145.20E	602	5.3

the dedicated deployment of broadband ocean bottom seismometer networks supported by the Japanese project 'Stagnant Slab Project' (Miyamachi *et al.* 2009; Shiobara *et al.* 2009) and the development of new tomographic methods (Fukao & Obayashi 2013; Obayashi *et al.* 2013). So, after this forced hiatus, we present here our original findings, which still constitute key observations due to the scarcity of deep large events in this region, augmented by new data from two additional events recorded at additional arrays (Section 4.1) and several new figures (Figs 13–17), which show that the results from our array analysis, using both *P* and *S* waves in contrast to previous publications, provide a location for a stranded slab that is in good agreement with recent high-resolution tomography.

On 1995 August 23, a large earthquake occurred at *ca.* 600 km depth in the central Mariana subduction zone; the first large deep earthquake in this location since the advent of University of California, Berkeley and California Institute of Technology broadband networks equipped with new generation seismic broadband instruments. In Fig. 1, we show the location of the deep Mariana earthquake (star) and the location of the California broadband instruments (triangles). A line connects each broadband station to the earthquake epicentre along a great circle path. Fig. 2 shows details of the study area in the Mariana subduction zone. The deep earthquakes from 1995 used in this study (Table 1) occur in a portion of the Pacific Plate that subducts at the Mariana trench—the dark blue arcuate bathymetric feature extending from the Caroline Ridge in the south to the OP-MN in the north.

An anomalous high amplitude seismic phase we refer to as the '*X*' phase was recorded at vertical broad-band California instruments for both this earthquake (Event 1; Figs 2 and 3a) and a large aftershock (Event 2; Figs 2 and 3b), see also Wicks *et al.* (1995, 1996, 1997) and Wicks & Weber (1996). The *X* phase arrives between the standard seismic phases *P* (the first arriving, initially downgoing *P* wave) and *pP* (the first arriving, initially upgoing *P* wave, that has reflected off the Earth's surface, Figs 3a and b). Although the California broadband stations have recorded what appears to be the *X* phase for other aftershock earthquakes following Event 1, the signal to noise ratio is much lower and the dominant period of the signal is much shorter than for the two largest earthquakes (Events 1 and 2), which we use to locate the secondary source of *X*. For this reason we use only the two largest events to analyse the *X* phase in detail. Because of the possibility of *S*-wave to *P*-wave mode conversion, several secondary sources are possible to explain the *X* phase, but because of the observation of the *SX* phase (an S-wave counterpart to the *X* phase) in the transverse records of Event 3 (Figs 2 and 3c, for details see also Fig. 7) that arrives between *S* and *sS* (*S* wave counter parts to *P* and *pP*) we are able to deduce which of the possible secondary sources of *X* is most likely.

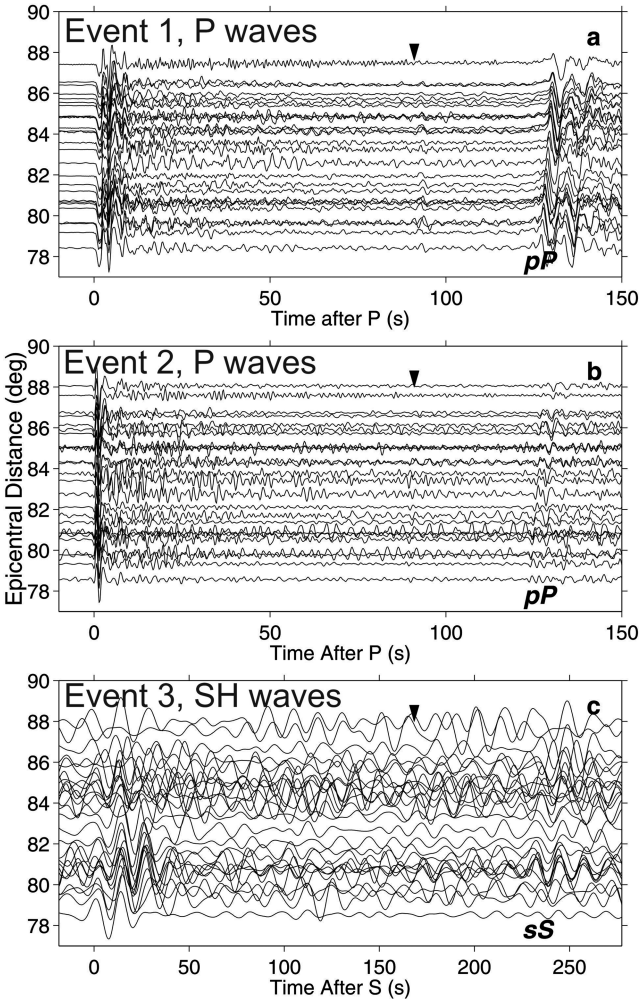

Figure 3. Record sections of data for event 1, 2 and 3. (a) Raw (demeaned) vertical velocity records of Event 1 data from 28 California broadband stations. Traces are aligned with the estimated onset of the *P* phase at $t = 0$. The arrow marks the approximate *X* phase arrival at 91s after *P*. (b) Filtered (bandpass 1 s–5 s) vertical velocity records of Event 2 data from 26 California broadband stations. Traces are aligned with the estimated onset of *P* at $t = 0$. The arrow marks the approximate *X* phase arrival. (c) Filtered (band pass 10 s–20 s) transverse velocity records (SH) of Event 3 data from 28 California broadband stations. The traces are aligned with the theoretical arrival time for S in an IASP91 earth model at $t = 0$. The arrow at 168 s after S (91 s multiplied by 1.85, a scale factor appropriate for an IASP91 earth model) indicates the approximate arrival time expected for an *S* to *S* (SH to SH) reflection from a 400 km deep reflector (Figs 2, 8, 9 and 12).

2 DATA ANALYSIS

To estimate the direction from California, to a secondary source for *X*, we use a delay and sum (beam forming) technique, processing the combined California broadband networks for each earthquake as a single array. By scanning different arrival directions we find that the seismic wave manifested as the *X* (*SX*) phase comes to California from a more northerly azimuth with a lower slowness than the wave manifested as the *P* (*S*) phase (Fig. 4). The slowness/backazimuth analysis results shown in Fig. 4 are the results of a grid search

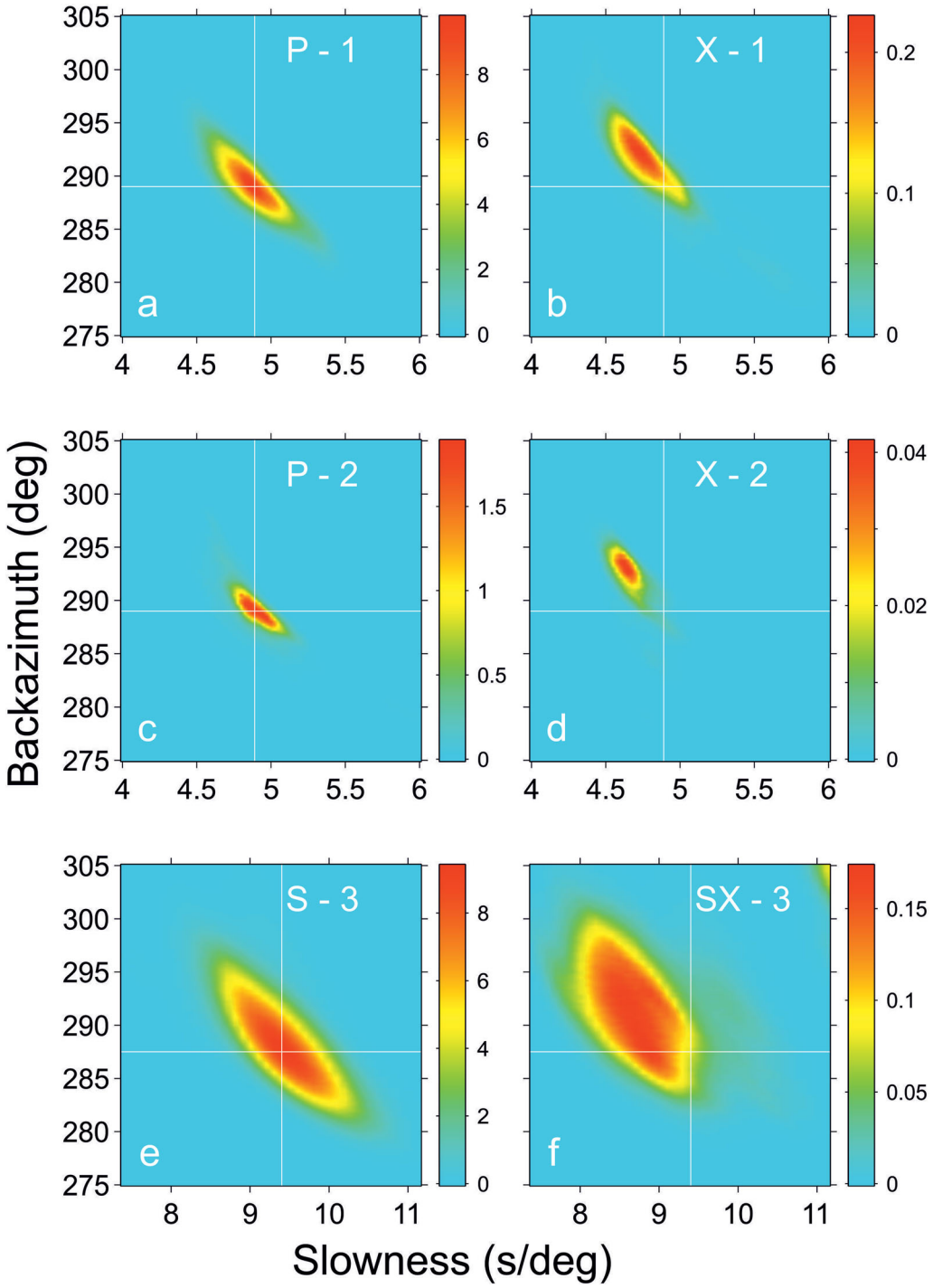

Figure 4. *N*th-root (Muirhead & Datt 1976, $N = 4$) beamform energy as a function of backazimuth and slowness. The white cross-hairs correspond to the slowness-backazimuth value where the maximum in *P* or *S* energy is found. (a) Event 1, analysis of 7 s window containing *P* phase data as (a). (b) Event 1, analysis of 7 s window containing *X* phase data as in (a). (c) Event 2, analysis of 6 s window containing *P* phase data as (a). (d) Event 2, analysis of 6 s window containing *X* phase data as in (a). (e) Event 3, analysis of 33 s window containing *S* phase data (SH) as in (a). (f) Event 3, analysis of 33 s window containing *SX* phase data as in (a). All *X* and *SX* phases arrive with reduced slowness and larger backazimuth relative to the reference phase (*P* and *S*), respectively, that is they arrive at the receivers from larger distance and more northerly.

procedure in which we start by adjusting each seismogram for Events 1 and 2 so that the reference phase *P* arrives at the expected time in an IASP91 earth model (Kennett & Engdahl 1991), effecting a station correction. We then time-shift the seismograms according to the slowness and backazimuth value under investigation, stack the portion of the seismograms that fall within the selected phase windows using an *N*th root (Muirhead & Datt 1976, $N = 4$) technique, then sum the squared amplitudes corresponding to the time samples within the phase window of the stacked seismogram. This is a modification of a method developed by Nakanishi (1988) that gives the *N*th-root energy at any slowness/backazimuth pair. By repeating this procedure for the slowness/backazimuth values in a

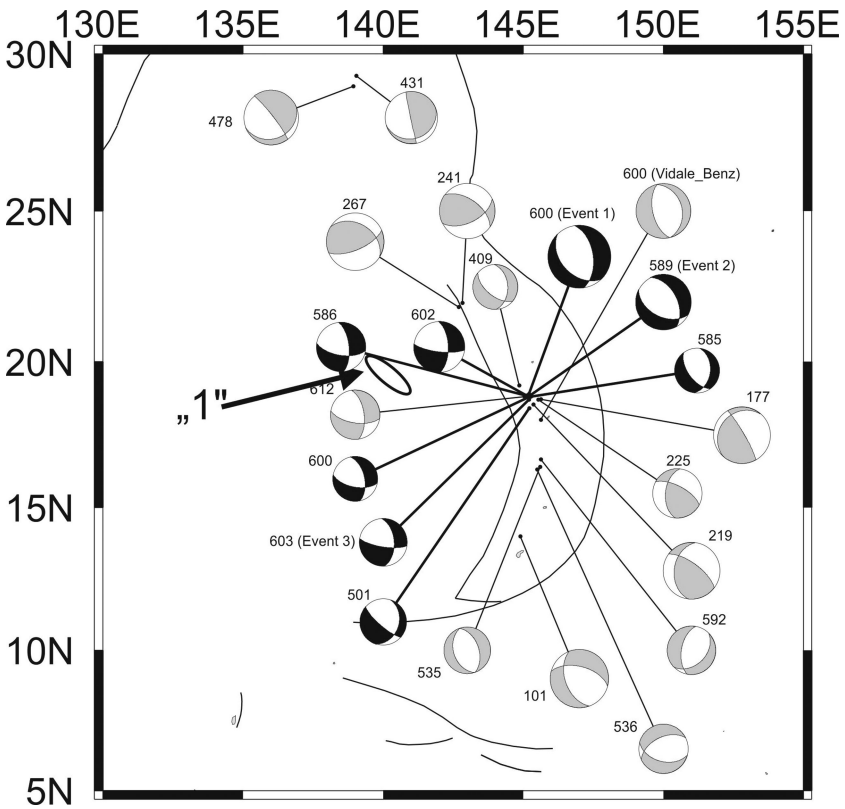

Figure 5. Location map of events in the vicinity of Events 1–3, marked with focal mechanisms derived from Harvard CMT solutions for events up to 1996. The thin lines are plate boundaries according to GMT (Wessel & Smith 1991). Events are labelled with hypocentral depth. All magnitudes are larger than m_b 5.0. The event labelled 'Vidale_Benz' is the event used by Vidale & Benz (1992). *X* and/or *SX* are exhibited in each event with a black focal mechanism, where *X* and *SX* are either absent or indeterminate in the grey focal mechanisms. The ellipse is the jack-knife error ellipse labelled '1' in Figs 2 and 8.

grid, we form the *N*th–root energy plots shown in Figs 4(a)–(d). The *N*th-root energy plots for Event 3 (Figs 4e and f) have been generated using the same procedure, except that the transverse records for Event 3 are too noisy, to affect the initial station correction using the reference *S* phase. Since the records for Event 3 have been bandpass filtered from 10 s to 20 s, the impact of skipping the initial station correction should be minimal.

Events 1 and 2 both exhibit good *X* and *P* phases, which proved easy to isolate with respect to slowness and backazimuth (Fig. 4), however finding an event with combination of easily isolated *SX* and *S* proved to be difficult. Since we reference the values of slowness and backazimuth found for *X* and *SX* to the reference phases *P* and *S*, it is important to find events which exhibit well isolated reference phases. Although events 1 and 2 were large, the radiation pattern for SH energy directed toward our preferred scatterer location is the best for Event 3. Only very small amplitude arrivals at the time of *SX* could be found in the transverse records of Events 1 and 2. The radial components for all three events contained significant energy from *SP*, *PS*, *SSP*, *sSP*, *sPS* and *PSS* type phases preventing a clear separation of *SX* energy. Event 3 was found to be the only event, of all the events we investigated, with well isolated *SX* and *S* phases. Because the 33 s time window used to analyse *S* in Fig. 4(e) also could include *ScS*, *SKSac* and *SKKSac*, it is important to note that the energy is a single peak, with no energy at slowness values of *ca*. 6.2 to *ca*. 8.2 s deg^{-1} that would correspond to these core phases. Vertical records of Event 3 exhibited low amplitude very short-period energy which probably was the *X* phase (it was interpreted as such and used by Kaneshima & Helffrich 1998). The short-period nature of the phase made it unuseable with the array and stacking method we use.

2.1 Aftershocks?

We use the following three lines of evidence to argue against the *X* phases being aftershocks:

(1) The traveltime difference between *X* and *P* is constant, within errors, for Events 1 and 2.

(2) The *X* phases for Events 1 and 2 come to California from a more northerly azimuth than the respective P phases (Fig. 4, ellipses in Fig. 2). This is verified by applying a jackknife resampling method to the data in Figs 4(a)–(d). In this method we process the California array for each event (1 and 2) M-1 times (where *M* is the number of records for each event). Each time the array is processed, one record is excluded in turn, until every record but that of our reference station PKD1 (the approximate array centre) has been excluded. The difference in backazimuth and slowness between *X* and *P* is found for each jackknife realization, and then added to the theoretical slowness and backazimuth of P in an IASP91 earth model. The resulting points for each event are enclosed by ellipses in Fig. 2. The green ellipse encloses the jackknife realizations for Event 2, and the red ellipses enclose the jackknife realizations for Event 1. The red ellipse labelled '1' and the green ellipse are projected at a depth of 400 km. A comparison of the two ellipses (red '1' and green) shows that they overlap, and that the size of the red ellipse is smaller than the green ellipse. The smaller size of the red ellipse

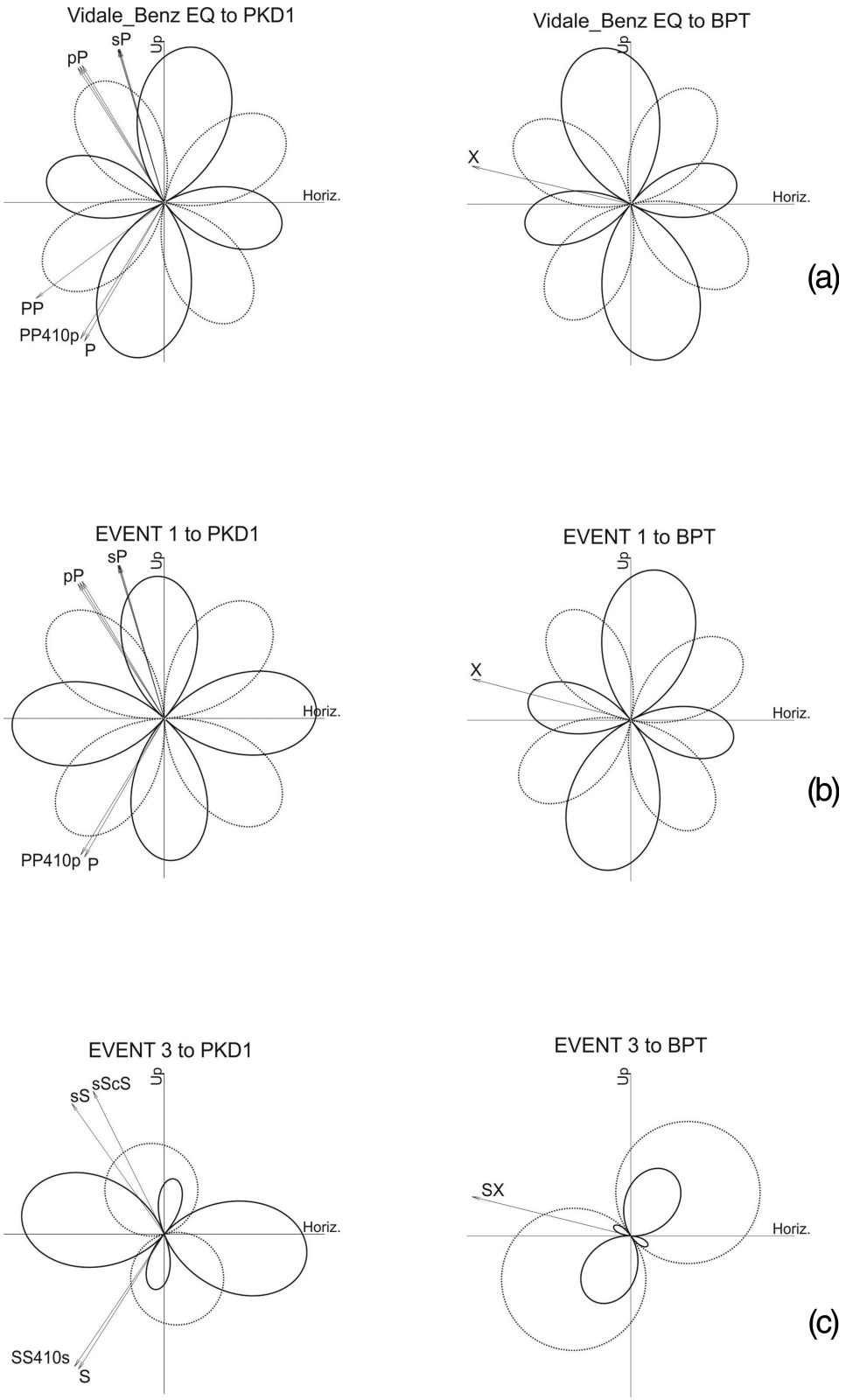

Figure 6. Source to receiver (station PKD1 in California) and source to scatterer number 1 (BPT, stands for bounce point) radiation patterns. Take-off vectors show the energy radiated along selected (labelled) phase paths. Left-hand panel: radiation for source to receiver sagittal plane. Right-hand panel: radiation for source to scatterer 1 sagittal plane. Solid lines denote *P*-wave radiation, dashed lines denote SV component of *S*-wave radiation. (a) Radiation patterns for Vidale and Benz event, discussed in text. (b) Radiation patterns for Event 1. (c) Radiation patterns for Event 3.

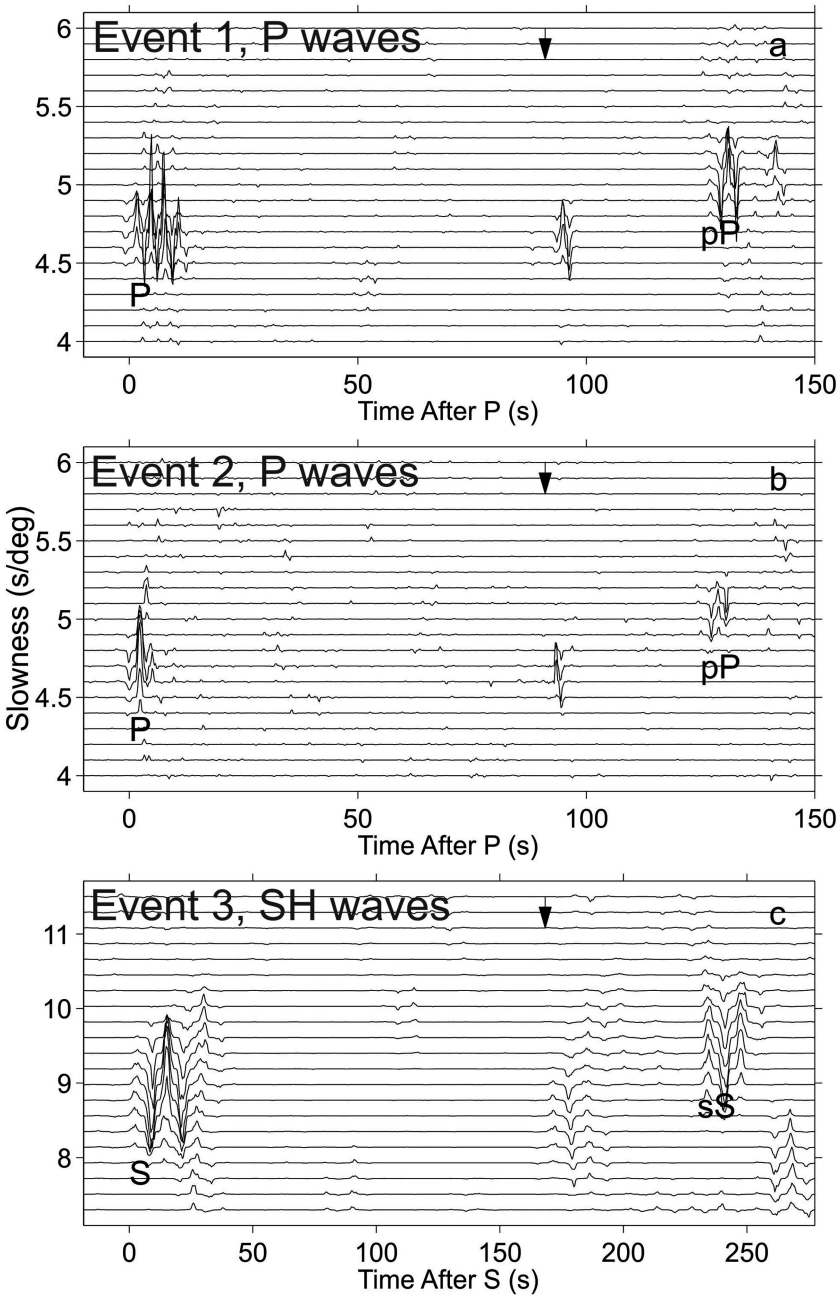

Figure 7. Vespagrams (Davies *et al.* 1971) for event 1, 2 and 3. Each vespagram has been processed at the backazimuth optimal for *X* or *SX* (Fig. 4) using the *N*th-root method (Muirhead & Datt 1976, $N = 4$). Prominent phases are labelled. (a) Event 1, bandpass filtered (1 s–5 s) of data shown in Fig. 3(a). Arrow as described in Fig. 3(a). (b) Event 2, data as shown in Fig. 3(b). Arrow as described in Fig. 3(b). (c) Event 3, *SH* waves, data as shown in Fig. 3(c). Arrow as described in Fig. 3(c). The time axis is scaled by the factor 1.85 (*Vp*/*Vs* ratio in IASP91 model, see also Fig. 3). The phase arriving after *sS* with a slowness of *ca*. 8 s deg^{-1} is *sScS*.

comes from the higher signal to noise ratio for Event 1 compared to Event 2 (Fig. 3).

(3) The *X* phases for Event 1 and 2 are absent on seismograms recorded by arrays at azimuths toward Europe, Asia and Australia.

2.2 Possible locations of secondary source for *X* and *SX*

Similar to Weber & Wicks (1996) we have used the directional information shown in Fig. 4 and the traveltime differences between *X* and *P* (Fig. 3) to estimate the location of a seismic structure that has served as the source for the *X* phases in an IASP91 earth model (Kennett & Engdahl 1991). We estimate that the secondary source for *X* is either a source side structure within one of the three red ellipses in Fig. 2, or a receiver side reverberation at a regionally tilted/warped 410-km discontinuity. The slowness, backazimuth and arrival time of the *SX* phase after *S* (Figs 3c and 4e–f) enable us to estimate the possible secondary source for *SX*, which can only be a structure in the upper mantle near the source (Fig. 2), or a receiver side reverberation as for the *X* phase. The possible receiver side reverberation *PP410p* (*SS410s*) leaves the source as a downgoing *P* (*S*) wave, reflects of the Earth's surface near the California coast,

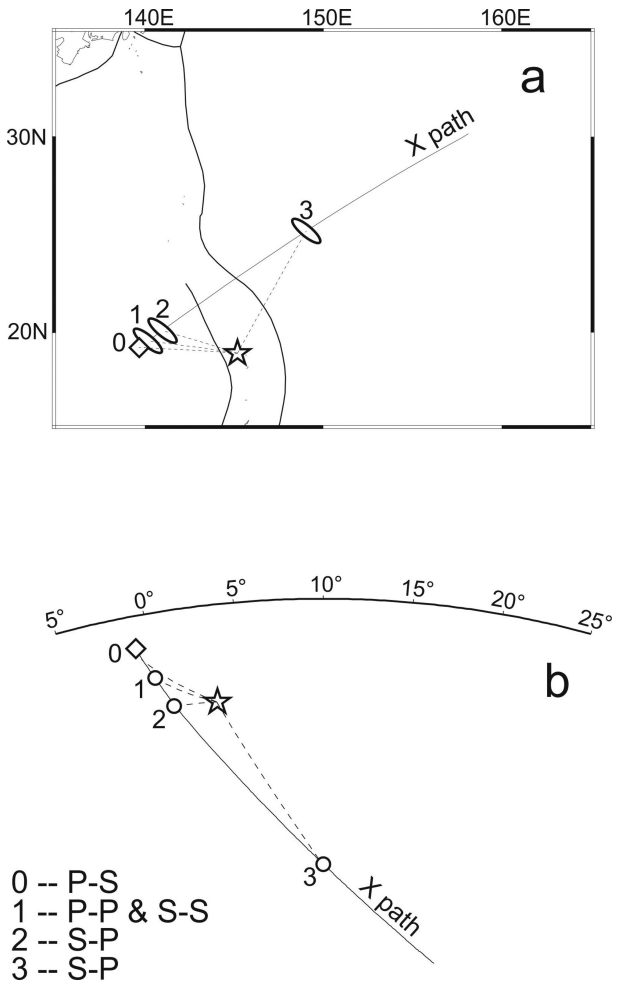

Figure 8. Projection of possible scatterer locations. The dashed lines are projections of rays from Event 1, marked with a star, to possible scattering locations (labelled symbols). The figure legend indicates the type of mode conversion (if any) takes place at each labelled scatterer (or secondary structure). (a) Map view of possible ray path geometry for all possible source side structures which could lead to the observed *X* or *SX* phases. The hollow diamond labelled '0' is a possible *P–S* scatterer at *ca*. 240 km depth. The hollow ellipse labelled '1' is our favoured reflector location near 400 km depth, valid for *P* and *S* (*SH*) waves. The hollow ellipses labelled '2' and '3' are other possible scattering locations which fit with *S–P* conversion scattering origins for *X* at 550 and 1600 km depth, respectively. This information is also in Fig. 2. (b) A cross-section on a plane through the great circle '*X path*' shown in (a) above and Fig. 2. The numbers labelling the hollow circles are as in (a) and in the figure legend. The earthquake is at a depth of *ca*. 600 km. Arc distance (labelled on top) is relative to the hollow circle labelled '1'.

travels down to the 410-km discontinuity where it reflects up to the stations in California. The only structures common to the *X* and *SX* observations are thus a near source reflector at 400 km depth (Fig. 2) or receiver side structure on the 410-km discontinuity.

2.2.1 Receiver side structure?

The receiver side structure on the 410-km discontinuity is an unlikely source for either the *X* or the *SX* phase for the following reasons:

(1) The large amplitudes of *X* and *SX* are difficult to explain with receiver side structure.

(2) The lack of observations of other such high amplitude phases from records of earthquakes outside of the aftershock area of Event 1 (Fig. 5). Except for earthquakes spatially related to the large Event 1 we have not found any other records with the characteristics of the *X* (*SX*) phase, but see also Section 4.1.

(3) The complexities of a phase like *PP410p* which should bear the signature of reflection off the ocean bottom/surface are not seen.

If the *X* and *SX* phases were near receiver reverberations from the 410-km discontinuity, the large amplitudes of *X* (*SX*) observed in our data would require an impedance contrast of more than 40 per cent across the 410-km discontinuity. Strong contrasts across the 410 have in fact been discussed by Bercovici & Karato (2003) and Karato (2011), but seismological studies indicate only a maximum drop of 5 per cent on top of the 410, especially for Northern California (Song *et al.* 2004). Another process producing large amplitudes could be focusing by a perturbation of the 410 km distributed across a region larger than California. This would focus *PP410p* (*SS410s*) waves for stations in California (and Washington, Kaneshima & Helffrich 1998), so we would expect to see the high amplitude *X* (*SX*) phases for shallower earthquakes and earthquakes near the aftershock area of Event 1 (Fig. 5), which we do not see. Moreover, the difference in take-off angle between *P* (*S*) and *PP410p* (*SS410s*) is less than 2° (Fig. 6), so events with high amplitude *P* (*S*) observations should also exhibit high amplitude *PP410p* (*SS410s*) phases. However, we do not see *X* or *SX* even in records of the largest earthquakes outside the aftershock area around Event 1. As an example: Vidale & Benz (1992) analysed a 1982 earthquake with a body magnitude of 6.1, at a depth of 600 km, and only *ca*. 100 km south of Event 1 (Fig. 5). Their analysis showed no energy which would correspond to *PP410p* even though it should have had amplitudes larger than the *pP* amplitudes they observed, if the *X* phase were *PP410p*, see Fig. 6(a) for the radiation pattern. Although Vidale & Benz (1992) looked for energy arriving from the same azimuth as *P*, energy at periods longer than *ca*. 1.5 s should stack constructively given the arrival direction we see for *X*, the linear stacking method they applied, the array they utilized and the data frequency band they applied in their investigation.

Another argument against a receiver side reverberation origin for *X* and *SX* is the simple waveform observed for *X* (Figs 7a and b). The phase *PP410p* should exhibit a complex waveform, with the complexities of *P* (because of the similar take-off angle) and additional complexities from interactions with suboceanic crustal structure and ocean water at the surface reflection point. However, as already noted, the waveforms of *X* are much simpler than the waveforms of *P* (Figs 7a and b).

Fig. 5 shows the earthquakes we examined for *X* and *SX* phases. The black focal mechanisms mark earthquakes for which *X* or *SX* were recorded in California as reported in this study [events 1 and 2 (X phase) and event 3 (SX phase)] or the study of Kaneshima & Helffrich (1998) with five more events. Records of the earthquakes marked with the grey focal mechanisms exhibited no discernible *X* or *SX* phase. Note in Fig. 5 the small area and depth range of earthquakes for which *X* and *SX* are observed.

2.2.2 Source side structure?

By virtue of the high signal to noise ratio (discussed above) the records of Event 1 yield the most accurate estimate of the direction to the secondary source for *X*. So, we search along the ray path of *X*, estimated from Event 1 records, for possible scattering points which could explain the *X–P* and the *SX–S* traveltime differences

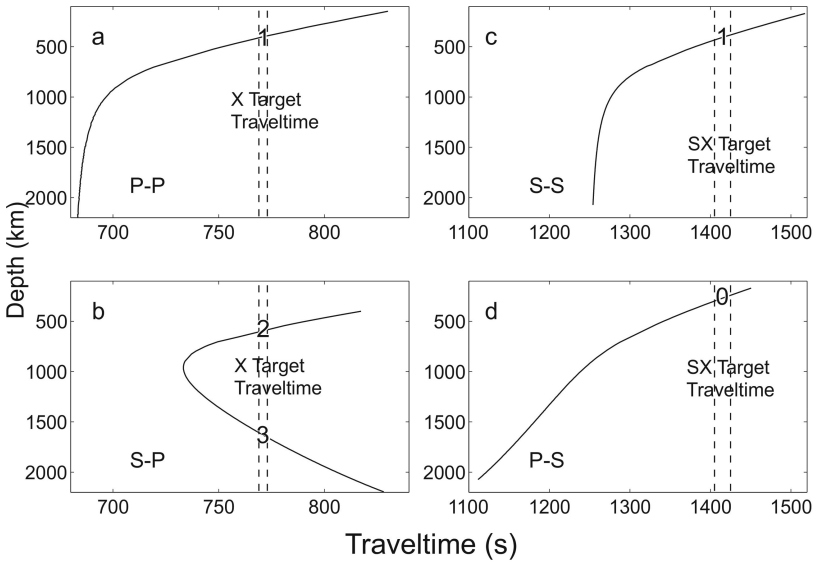

Figure 9. Calculated traveltime (given the geometry in Fig. 8) from the earthquake source, to possible scatterers along the optimum ray path found for Event 1, labelled '*X Path*' in Fig. 8. The target traveltime for *X* and *SX* have been read from the seismograms, and are shown as vertical dashed lines indicating the traveltime uncertainties. The labels at each intersection of the traveltime curve with the target traveltime region correspond to the scatterer locations shown in Fig. 8. (a) *P* wave to *P*-wave scatterers. (b) *S* wave to *P*-wave scatterers. (c) *S* wave to *S*-wave scatterers. (d) *P* wave to *S*-wave scatterers.

(Fig. 7). The ray path for *X* that we search is shown in Figs 2 and 8 and labelled '*X path*'. The star in Fig. 8 marks the location of Event 1 in plane view in Fig. 8(a), and in cross-section along the *X* path in Fig. 8(b). We now calculate the traveltime for the four possible elastic wave scattering scenarios, for a wave leaving the source, scattering at points at different depths on the '*X path*' to the receivers in California. In Fig. 9, we show a comparison of the calculated traveltimes to the observed traveltimes of *X* and *SX*. Four possible scatterer locations are found, which we show in Figs 2, 8 and 9, labelled '0', '1', '2' and '3', respectively.

(1) Location '0': This location fits slowness, backazimuth and delay time of *SX* observed for Event 3 if a *P*-wave is reflected/diffracted at location 0 as an *S* wave. One argument against this scenario is that the *P* could not efficiently convert to SH energy for this geometry. However, the main argument against a scatterer at '0' is that Events 1 and 2, which both have good *P* radiation towards this location, do not show arrivals that would be produced from a *P*–*S* reflection.

(2) Location '1': This location is a possible *P to P* and also *S to S* reflector/diffractor which explains the observation of the *X* phases and also the *SX* phase. Fig. 6(b) shows that the *P*-wave radiation for Event 1 is peaked along a ray to this location. The *P*-wave radiation for Event 2 (not shown) is similarly peaked, but the peak amplitude on the radiation lobe toward location 1 is reduced by about 40 per cent. Fig. 6(c) shows that substantial *SH*-wave energy is radiated in the direction of this possible scatterer. This is our preferred location.

(3) Location '2': This is the location of a secondary source for *X* through reflection/diffraction of *S* to *P* wave converted energy. If there were a seismic impedance anomaly in location '2', Event 3 should have an arrival *ca*. 100 s after *S* from an *S*–*S* reflection. *SX* however arrives *ca.* 165 s after *S* for Event 3 (Fig. 3c).

(4) Location '3': This is the location of a secondary source for *X* through transmission/diffraction of *S*- to *P*-wave converted energy. This is the scattering scenario advanced by Kaneshima & Helffrich (1998). For this location to be the true secondary source for *X*, all shallow events above Event 1 should also show the *X* phase, since the ray paths to location 3 are very similar to those for the deep events (Figs 6 and 8). However, *X* phases are not observed for the shallow events—additional evidence that location 3 is not the secondary source for *X*.

Thus of the four locations listed above, only location 1 is the location for a seismic anomaly that could be a secondary source for both *X* and *SX*, that is for *P* and *S* (*SH*) waves. It is important to note also from Figs 9(c) and (d) that a secondary source for *SX* cannot be located in the lower mantle.

The *P*-wave and *S*-wave vespagrams in Fig. 7 are constructed in such a way that the *X* and *SX* should be similar, if they have a common secondary source at location 1. The vespagrams for *X* in Figs 7(a) and (b) have the same range of slownesses and time and they have been processed at the backazimuth where the peak energy for *X* is found in Figs 4(b) and (d). The range of slowness in the vespagram for *SX* (Event 3) in Fig. 7(c) has been chosen to correspond to the range of slownesses for *P* waves shown in Figs 7(a) and (b), based on an IASP91 earth model. The time interval in Fig. 7(c) (*S* waves) is the same as those for the *P* waves, multiplied by 1.85, the ratio of *P*- to *S*-wave velocity in the IASP91 model in the upper mantle. The arrows in Figs 7(a) and (b) are placed to mark the approximate arrival time of *X* in event 1 (*ca*. 91 s after *P*) and the arrow in Fig. 7(c) marks the expected arrival time for *SX* estimated by multiplying 91 s by 1.85, that is 168 s. Event 3 is located close enough to Event 1 so that the three vespagrams only look similar if *X* and *SX* have the same secondary source at location 1 (Figs 2, 8 and 9). That is the two independent observations (*P* waves: *X* phase and *S* waves: *SX* phase) can only be explained by a common scattering/reflecting object in location 1.

3 INTERPRETATION AND DISCUSSION

Because of the large amplitudes of *X* and *SX* and small source region for the phases (Fig. 5), we argue that it is more appropriate to consider the anomalous phases as reflected energy rather than scattered energy, and we interpret this reflector to be a piece of

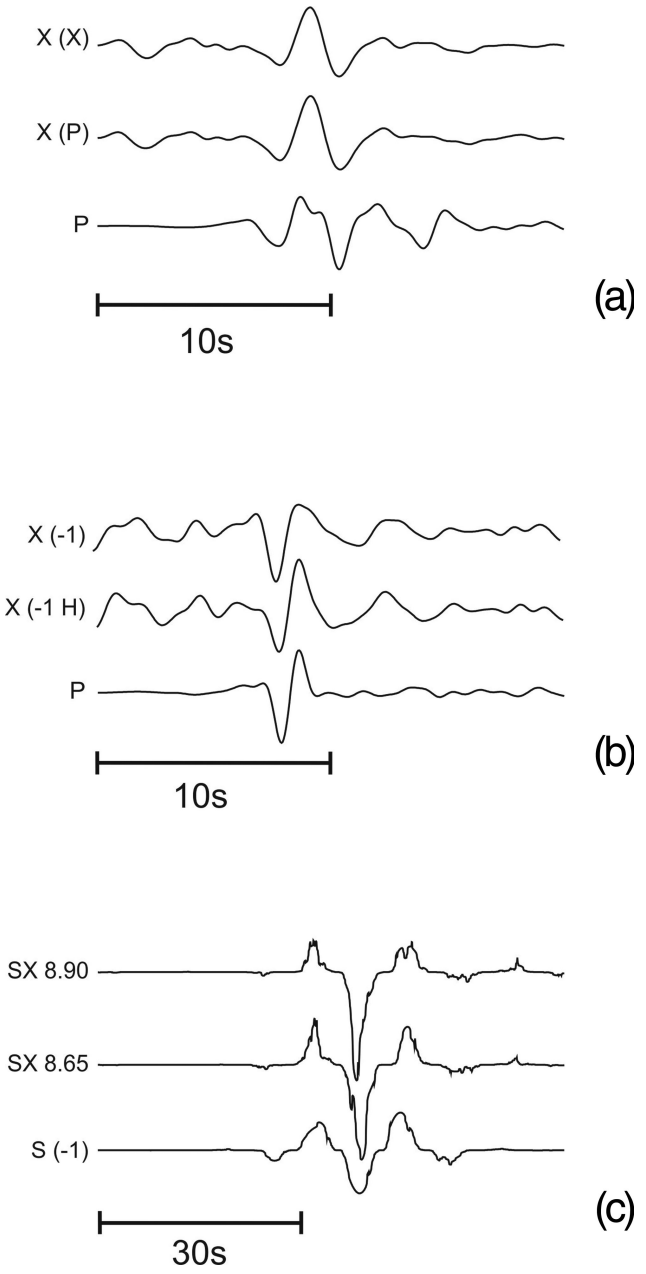

Figure 10. Comparison of *P* (*S*) and *X* (*SX*) waveforms. (a) Linear stack of 28 filtered vertical seismograms of Event 1, used in Figs 4(a), (b) and 7(a). The traces of the *X* phase [labelled 'X(X)' and 'X(P)'] are shifted 91s with respect to the trace of the *P* phase. The trace labelled *X*(X) has been normalized on *X* before stacking. The trace labelled *X*(P) has been normalized on the *P* phase, stacked, then magnified 7.3 times relative to the trace of *P*. The phase arriving *ca*. 6 s after *P* is most likely the phase $S_{660}P$. (b) Linear stack of 26 filtered vertical seismograms of Event 2, used in Figs 3(b), 4(c), (d) and 7(b). The two traces of the *X* phase [labelled 'X(−1)' and 'X(−1 H)'] have been normalized on the *P* phase, stacked, then magnified nine times with respect to the trace of *P*. The trace of *X* labelled 'X(−1)' has been phase reversed and shifted 90.3 s with respect to the trace of *P*. The trace of *X* labelled 'X(−1 H)' has been Hilbert transformed, phase reversed, then shifted 89.8 s with respect to the trace of *P*. (c) *N*th-root ($N = 4$) stacks of 28 filtered transverse seismograms of Event 3, used in Figs 3(c), 4(e), (f) and 7(c). The two traces of *SX* (labelled '*SX* 8.90' and '*SX* 8.65', where the numbers 8.90 and 8.65 indicate slowness value used), have been normalized on *S*, stacked, then magnified 10 times relative to *S*. Each *SX* trace is also shifted 165 s relative to the *S* trace. The trace of *S* [labelled 'S(−1)'] has been phase reversed.

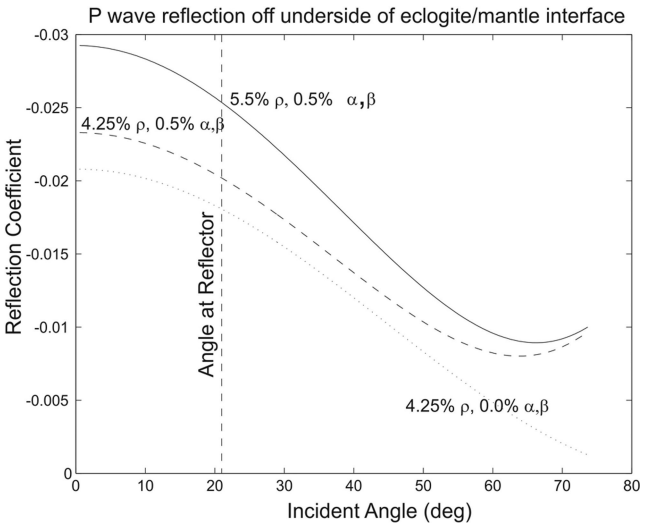

Figure 11. Reflection coefficient for a *P* plane wave reflecting off the underside of a normal mantle/Eclogite interface (mantle above, Eclogite below) as a function of incidence angle. The geometry is that shown for scatterer 1 in Fig. 8 and for the proposed slab segment in Fig. 12.

stranded (or at least slowly sinking) slab material or remnants of such a process. Assuming we can neglect the effects of geometrical spreading and attenuation (which is good to *ca*. 10 per cent) we can estimate the reflection coefficients, given the radiation patterns shown in Fig. 6 and the stacked seismogram amplitudes shown in Fig. 10. The estimated reflection coefficients using the *X* and *P* phases are 8 per cent for Event 1 and 10 per cent for Event 2. Using the *SX* and *S* phases (SH) from Event 3, we estimate a reflection coefficient of 15 per cent. These reflection coefficients require velocity and density anomalies of at least 10 per cent under the assumption of a tabular reflector (see also Fig. 11). Smaller bodies would require even larger contrasts of velocity and density. We note that *P* velocity contrasts of 5–12 per cent have been inferred at near 400 km depth in other subduction zones (Fukao *et al.* 1978; Gubbins & Snieder 1991). The reflector over scatterer scenario is supported by the fact that *X* and *SX* phases are not observed in records of shallower events above *ca*. 500 km depth (Fig. 5). If the reflector extended up to a depth of only *ca*. 300 km and the *X* and *SX* phases in Events 1–3 were dominantly reflected energy, observations of *X* or *SX* would not be expected for the shallower events in Fig. 5. The inferred reflector is centred at a depth of *ca*. 400 km, strikes *ca*. 7° west of north and dips *ca*. 40° to the west (Figs 2, 8 and 12). We estimate this geometry using ray theory and Snell's Law in an IASP91 earth model.

We interpret the imaged reflector to be a segment of slab (subducted oceanic lithosphere) or remnants of it that is most likely related to a previous episode of back arc spreading in the Mariana margin. To estimate the effects of curving a 2-D slab and thereby gain better understanding of velocity and density anomalies required by the data, we have investigated the effect of a curved slab on the X amplitudes by calculating Gaussian beam waveforms (Weber 1988; Davis & Henson 1993) for a construction similar to the 3-D problem in our study. We found that by curving the model slab, concave toward the receiver, a reflection coefficient (RC) as small as 2 per cent may be sufficient to produce the large amplitude *X* phases. Along strike curvature of the slab could lead to an even lower estimate of the required RC.

Even if the inferred slab segment is thermally equilibrated the density contrast between the top of the subducted slab [formerly

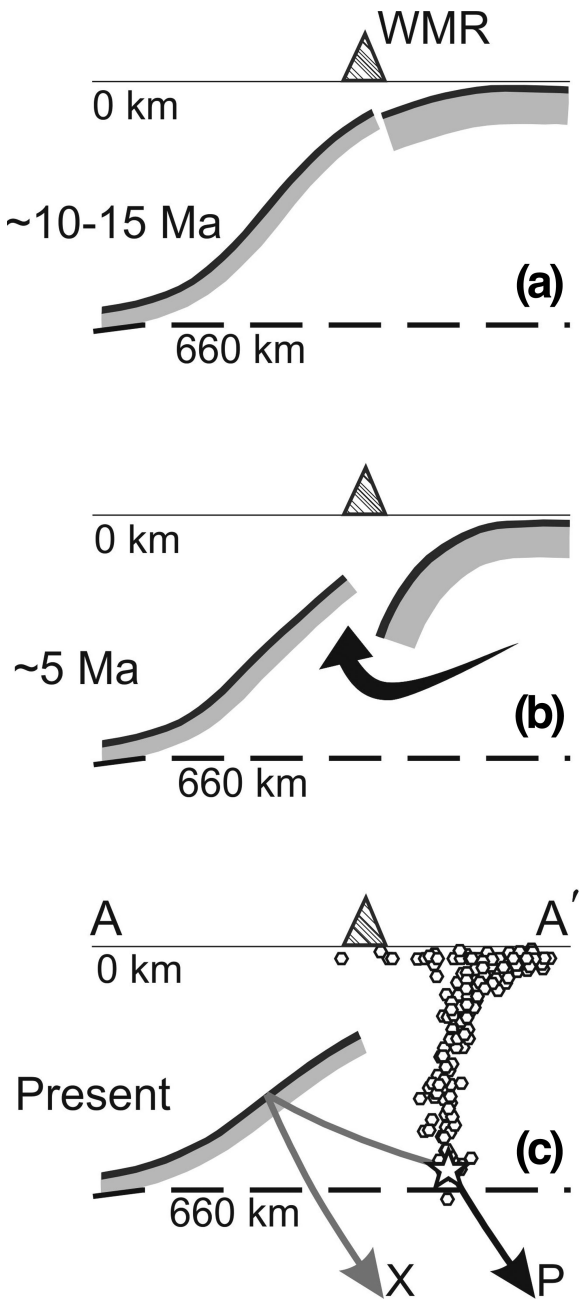

Figure 12. Schematic diagram, showing the speculative sequence of events leading to the stranded slab we have inferred. The triangle labelled WMR marks the position of the West Mariana Ridge, which is speculative in (a) and (b), but known in (c). (a) Rifting of the slab along the subducted suture. (b) Re-initiation of subduction accompanied by initiation of back-arc spreading in the Mariana trough and a new source of K-rich mantle material (Lee *et al.* 1995), marked with the arrow. (c) Composite cross-section illustrating our interpretation of the imaged reflector. The plane and limits of the cross-section are shown with the red line labelled A–A′ in Fig. 2. The cross-section is taken parallel to the dip direction of the modelled reflector. The black arrow labelled P shows the projection of the ray for *P* and *S* to California in an IASP91 earth model; the arrow also corresponds to the surface projection of the ray for *P* (*S*) labelled GC path in Fig. 2. The grey arrow, labelled *X*, shows the projected path of the ray for *X* and *SX* in an IASP91 earth model, which corresponds to the dashed line labelled *X* path in Fig. 2—the surface projection of this ray. The hexagons are the hypocentre locations of earthquakes used in Fig. 2, plus shallow earthquake hypocentres, that fall within 1° of a plane parallel to the cross-section, but passing through the hypocentre location of Event 1.

basaltic crust now most likely composed of garnetite (Irifune & Ringwood 1993)] and the overlying peridotitic mantle should be about 4.25–5.5 per cent (Irifune & Ringwood 1993). The olivine to spinel phase transition produces a 4–8 per cent velocity contrast around 400 km depth at the interface between the subducting slab and the ambient mantle above, according to Helffrich *et al.* (1989). Kono *et al.* (2012) find, that MORB transforms to garnetite near the 410-km discontinuity with *Vp* and *Vs* lower by about 2 and 5 per cent, respectively than those of reference models. Another explanation for the reflector might be that metastable olivine of the subducted slab is still present below the 410, similar to the metastable olivine wedge beneath SW Japan found by Kawakatsu & Yoshioka (2011). As we show in Fig. 11, even significant smaller velocity contrasts than those postulated above, combined with a larger density contrast, would yield a RC of more than 2 per cent for the source–reflector–receiver geometry we have estimated. A reflection at the bottom side of the oceanic crust could therefore yield significant reflection coefficients and thus explain the *X* and *SX* phases, respectively.

The observed polarity of *X* and *SX*, compared to *P* and *S*, respectively, can be explained by bottom-side reflection at the interface between the top of the subducted oceanic crust and the lower velocity, less dense mantle above. The polarity of *X* and *P* appear to be the same in Fig. 10a. Note that we interpret the phase arriving after *P* to be the phase $S_{660}P$, which has been found to have amplitudes larger than *P* in some studies (Wicks & Richards 1993). The polarity of *X* compared to *P* is indeterminate for Event 2 (Fig. 10b). In fact the polarity of *P* best matches the phase reversed Hilbert transform of *X* (Fig. 10b, bottom two traces). Since the transverse records for Event 3 are noisy (Fig. 3c), we compare the waveforms of the *N*th-root ($N = 4$) stacked seismogram for *SX* and *S*. Since the *SX* energy in Fig. 4(f) is double peaked, we show two stacked seismograms of *SX* corresponding to the two peaks. The *N*th-root waveform characteristics (peaks and valleys) are similar to the phase reversed waveform of *S*, which is expected for the Eclogite/mantle interface we have developed.

We speculate that the reflector may be the last subducted portion (tail) of the North New Guinea (NNG) Plate (Seno 1984, 1985; Seno & Maruyama 1984), a plate proposed by Seno in his model of tectonic evolution for the western Pacific. In Seno's model, a tectonic suture between the NNG plate and the Pacific Plate with an age difference of *ca*. 50 Myr between the younger NNG Plate (*ca*. 50 Myr old at the time the suture was subducted) and the Pacific would have been subducted *ca*. 20 Ma. The nature of the suture is also speculative, but it would provide a weak zone for strain accumulation, which may have led to a rifting of the subducted plate, and a re-initiation of subduction. We illustrate the process schematically in Figs 12(a) and (b). Fig. 12(a) shows subduction of the suture with the age step, with the location of the then active volcanic arc—the West Mariana Ridge marked with the triangle labelled 'WMR'.

Lee *et al.* (1995) found a strong peak in explosive volcanism in the Mariana margin area, recorded in the subsea tephra record from *ca*. 16 Ma; this peak in volcanism could be related to the initial rifting of the subducted suture between the NNG and Pacific plates. A change in the mantle source of volcanic material was also proposed by Lee *et al.* (1995), nearly coincident with the peak in explosive volcanism. More recently Nelson *et al.* (2013) also found evidence for subduction related fluids in the PVB (see Fig. 2). A rifted slab could provide a window to a new mantle source (Fig. 12b); this is not in disagreement with regional isotope data used to infer an Indian Ocean reservoir isotopic signature to the Mariana trough basalts,

since the eastern extent of the Indian Ocean mantle reservoir is not known (Hickey-Vargas *et al.* 1995).

The re-initiation of subduction and sinking of the Pacific Plate led to the formation of the now active Mariana backarc basin (between the WMR and the Mariana trench, Fig. 2) and the Mariana volcanic arc. Fig. 12(c) illustrates our interpretation of the present situation. The position of the subducted Pacific Plate is inferred from the hypocentres marked by the hexagons. The *P* and *X* phase geometries, we have developed above are shown and labelled.

4 NEW EVIDENCE FOR A STAGNANT SLAB

4.1 More recent events

Since the events in 1995 discussed above, two larger events in the source area have occurred in 2002 and 2013, respectively (Table 2). We have analysed these two events at the following arrays, sorted by azimuth, see Fig. 13. We analysed the *P* and the SH wave fields from these (and additional, smaller events) at the arrays shown in Fig. 13. In none of the events was the radiation favourable for the SX phase.

GRF/GRSN, Germany has a source-receiver distance of *ca*. 100°, that is for these deep events *P* is too close to, or already in the core shadow. Furthermore we are at an unfavourable angle relative to the reflector, thus we could not observe the *X* phase. The JArray, Japan has a distance of *ca*. 15–35°, that is the wavefield is complicated by upper mantle triplications and 'strange' phases (manuscript by D. Suetsugu, JAMSTEC in preparation), but not from 'our reflector' due again to unfavourable azimuth. Eastern US (USArray), USA is at a distance of *ca*. 110–120° for the 2013 event, that is the array is already deep in core shadow. For the WRA (Warramunga Array), Australia the distance is *ca*. 45° and the azimuth is unfavourable (Fig. 13) so we cannot observe the *X* phase, but note the converted phases in the Mariana slab itself (Krüger *et al.* 2001). This leaves the Western U.S. arrays and YKA (Yellowknife Array), Canada. Results from those arrays are now presented.

Fig. 14 shows the vespagrams for the 2002 and 2013 events (Table 2) at the new, larger Californian array with 37 and 117 stations remaining after careful quality control, respectively. Here we show the vespagrams (similar to Fig. 7) aimed at the X phase. Event 4 (2002, Fig. 14a) only has an m_b of 5.7, thus the data quality is not as good as for event 1. Relative to *P*, the *X* phase has a backazimuth 4° larger (more northern) and a slowness *ca*. 0.3 s deg^{-1} smaller, as expected. The traveltime delay of the *X* phase is 104 s, instead of the 94 s shown in Fig. 7. We attribute this to a possible error in the source depth given in the CMT catalogue. ISC gives a source depth for event 4 as 634 km, versus 609 km in the CMT catalogue. The larger depth (634 km) agrees with the pP delay time in Fig. 14(a). For a source at 634 km depth we expect the *X* phase to arrive *ca*. 101 s after *P*. The deviation of 3 s compared to the data

Table 2. Earthquake information from USGS/HRVD CMT catalogue—additional events.

Event	Origin (yr/m/d:hr:mn:s)	Lat (°)	Lon (°)	Depth (km)	M_w
4	2002/01/07:13:26:31	19.03N	145.08E	609	5.9
5	2013/05/14:00:32:29	18.67N	145.35E	605	6.8

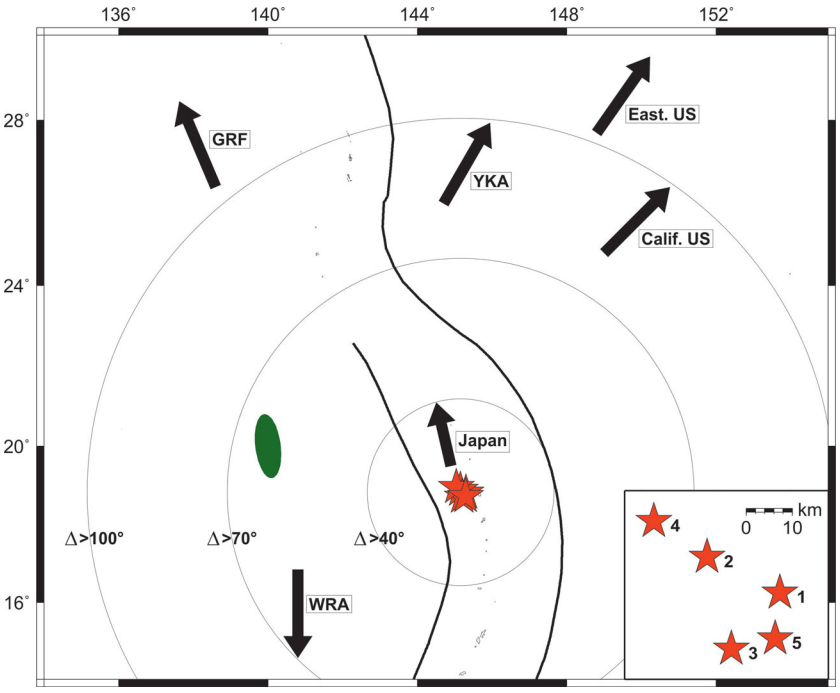

Figure 13. Study area with all five events used (Tables 1 and 2), red stars. Note insert with local blow-up of source area. The green ellipse is the location of the reflector. The arrows with labels show the azimuths for the reflector to the seismic arrays; GRF, Gräfenberg Array and the German Regional Seismic Network in Germany; Japan, JArray in Japan; YKA, Yellowknife Array in Canada; East. US, USArray in Eastern US in 2013; Calif. US, Californian Array and USArray stations at West Coast; WRA, Warramunga Array in Australia. The circles with labels illustrate typical distance ranges to the arrays analysed.

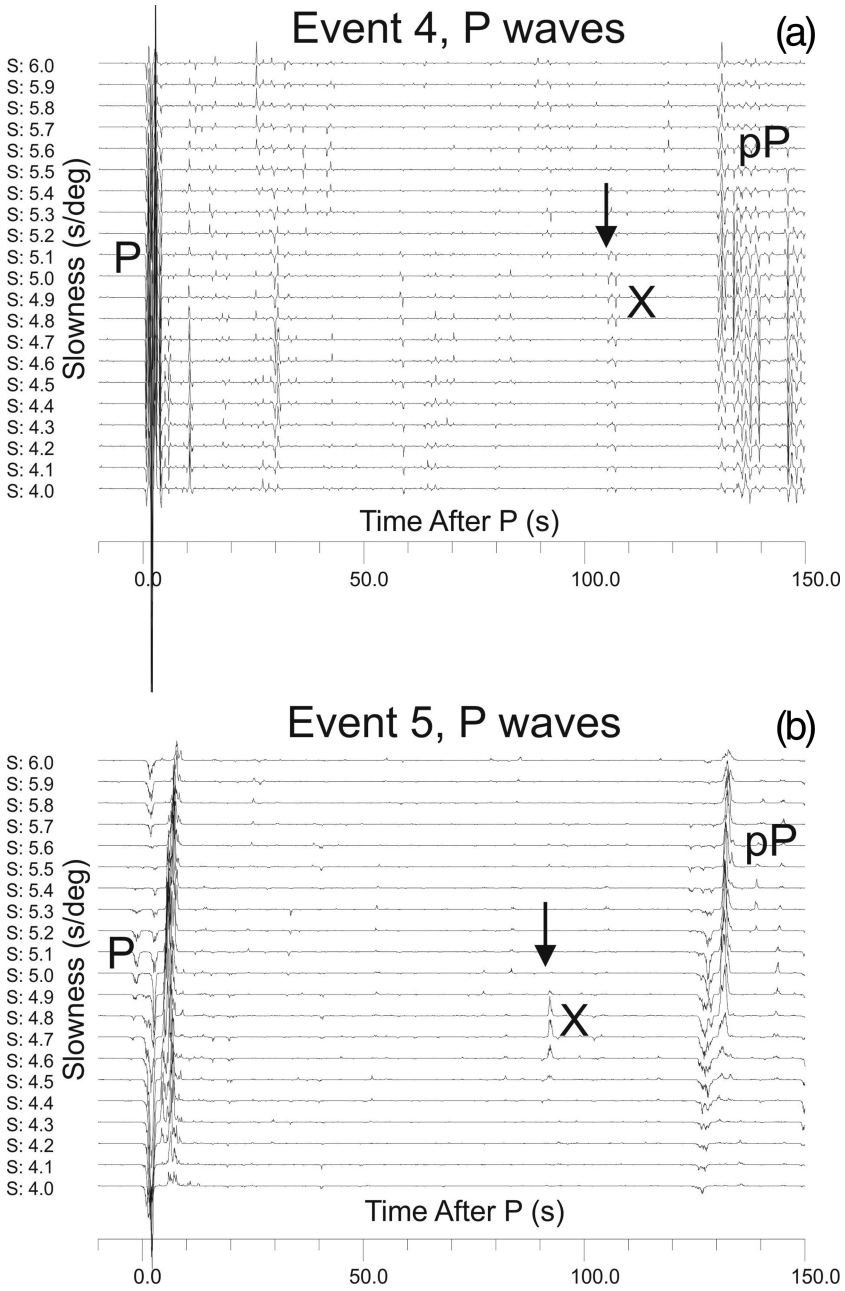

Figure 14. Vespagrams (Davies *et al.* 1971) for event 4 and 5 recorded in California. The usable network comprised 37 to 117 stations, respectively. Each vespagram has been processed at the backazimuth optimal for *X* using the *N*th-root method (Muirhead & Datt 1976, $N = 4$). Prominent phases are labelled. (a) Event 4, bandpass filtered (0.5–2 s). Arrow as described in Fig. 3(a). The observed value of the *P* slowness is 4.6 s deg^{-1}, the backazimuth of *P* and *X* is 288° and 292°; strike/dip/rake of this event is NP1 349/44/-82°, NP2 158/47/-98°, respectively. (b) Event 5, unfiltered. The observed value of the *P* slowness is 4.6 s deg^{-1}, the backazimuth of *P* and *X* is 289° and 291°; strike/dip/rake of this event is NP1 14/39/-30° NP2 124/68/-135°, respectively.

(104 s) seems acceptable, considering the traveltime variations produced by the strongly lateral inhomogeneities of the Marianas slab in the source region.

Fig. 14(b) shows the *X* phase as observed for event 5 (2013, Table 2) in California. Since in 2013 we could use 117 stations, instead of 37 in 2002, and since the 2013 event was significantly larger then event 4, the data quality is also superior. The delay time, backazimuth and slowness relative to *P* are as expected, for the reflector proposed, that is 93 s later, 4° larger (more northern) and 0.3 s deg^{-1} smaller than for direct P, respectively. This corroborates our previous findings, see the data of the closest previous event, event 1 (Fig. 7a) and Fig. 13 for the location of event 1 and 5.

An additional line of evidence for the reflector proposed comes from observations at the YKA (Yellowknife Array) in northern Canada. The distance to the Marianas is similar as to California but the azimuth is more northerly. Fig. 15 shows the vespagrams for event 1 at YKA. Due to the small size of the YKA array, we do not have the good resolution attained by the larger Californian array. Nevertheless we identify an *X* phase 86 s after *P* (see Fig. 15). This is the expected arrival time for the *X* phase from the proposed reflector. The time is *ca.* 7 s smaller than the 93 s for the propagation to California for event 1, in agreement with the different propagation path to YKA, compared to California.

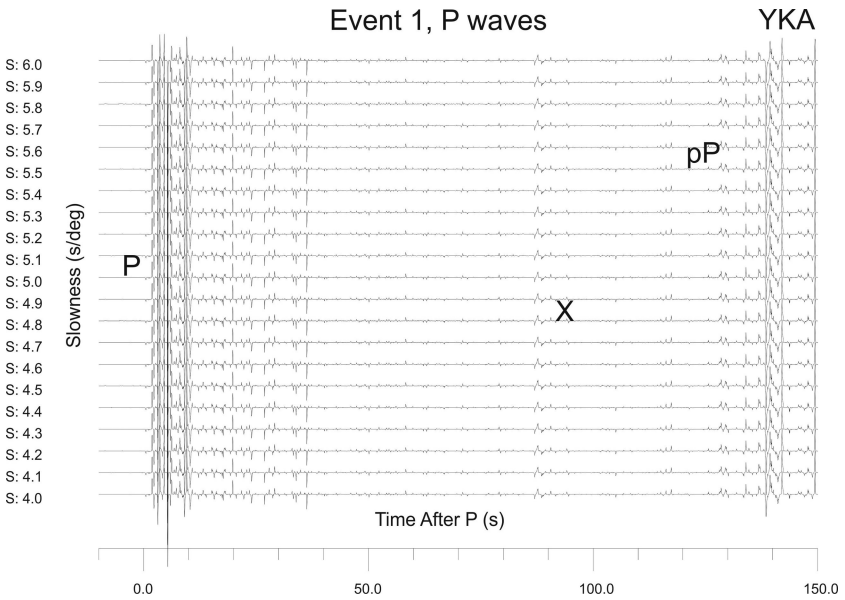

Figure 15. Vespagrams (Davies *et al.* 1971) for event 1 recorded at the YKA array (Yellowknife Array) in Canada. The vespagram of the unfiltered data has been processed at the backazimuth optimal for *X* using the *N*th-root method (Muirhead & Datt 1976, $N = 4$). Prominent phases are labelled. The observed value of the *P* slowness is 5.1 s deg^{-1}, the backazimuth of *P* and *X* is 288° and 289°, respectively.

In summary we conclude that two more usable events (2002 and 2013, respectively) and observations at another array (YKA) support our explanation of the *X* phase as originating at a reflector as shown in Fig. 12.

4.2 New tomographic studies

Previously, the only other seismic studies that have investigated the area near location 1 were tomography studies by van der Hilst *et al.* (1991) and van der Hilst & Seno (1993). A weak velocity anomaly was apparent in their regional tomography studies that appears to correspond to the reflector in location 1. A significant improvement in resolution of this area was shown recently in Obayashi *et al.* (2013) and Fukao & Obayashi (2013). By combining ray theory and finite frequency kernels for broadband waveform data, they were able to image slabs in the MTZ with unprecedented clarity. Fig. 16 shows a tomographic cross section through the GAP_P4 model (Obayashi *et al.* 2013), along profile A–A′ from Fig. 2, down to a depth of 700 km. We have overlain the results from Fig. 12(c) (present situation: reflector, event location and ray path of the *X* phase,) over the tomography. Note that this configuration holds not only for the *P*-wave path, but also for the *S*-wave (SH) path. The surprisingly good spatial coincidence of these two independent methods, tomography and array seismology [*P* and *S* waves (SH)], supports our conclusion, that this region of the MTZ contains a stagnant slab.

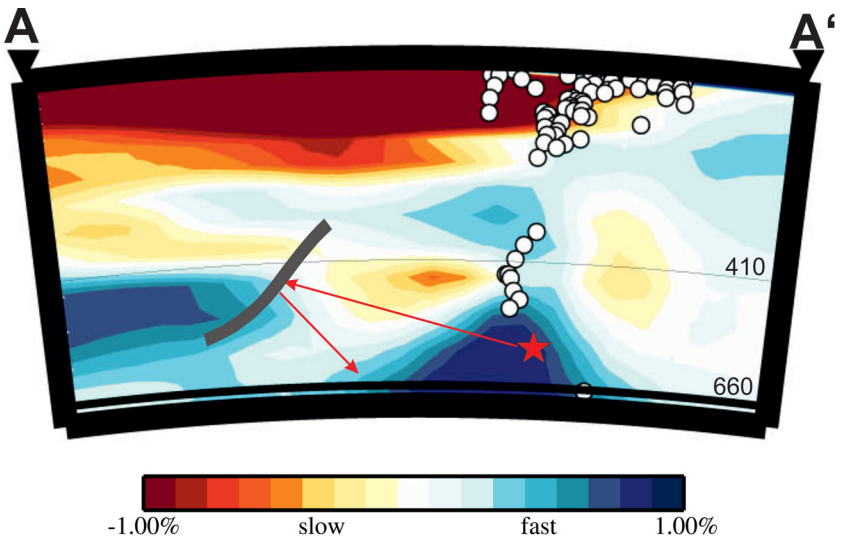

Figure 16. Tomographic cross-section through the GAP_P4 model (Obayashi *et al.* 2013) along profile A–A′ from Fig. 2, down to a depth of 700 km. The 410 (660) discontinuity is indicated by a thin (thick) black line, respectively. The open circles indicate earthquakes from Obayashi *et al.* (2013). The slab-like reflector (grey), Event 1 (red star) and the arrows indicating the ray paths of the *X* phase, are from Fig. 12(c), respectively. The tomographic image is courtesy of M. Obayashi.

We would like to point out, that tomography shows more voluminous, weaker and averaged velocity anomalies, whereas our reflection and array procedure is sensitive to impedance contrast of thin tabular anomalies. With the reflections in Figs 3, 4, 7, 10, 14 and 15 we might therefore be imaging the tail/dredges of the slab, not visible in tomography.

Additional evidence for a strong scatterer above the 660-km discontinuity west of the present day Mariana arc comes from Rost *et al.* (2008, their fig. 8a), which also shows significant azimuthal deviations from the great circle path between in and outgoing PP-precursors in this region.

We also estimated the possible effects of the slab proposed here on gravity. The signal expected will be less than 10 mGal, (P. Klitzke and L. Scheck-Wenderoth personal communication), that is a signal not detectable at the corresponding wavelength above the complex mantle west of the Marianas, see for example Obayashi *et al.* (2013) and Fig. 16 for images.

Independent confirmation that modern tomography (Fukao & Obayashi 2013; Obayashi *et al.* 2013) and seismic array techniques can nicely complement each other in imaging the mantle with unprecedented resolution also comes from Krüger *et al.* (2001). They used similar non-standard arrivals as the *X* phase, to locate two scatterers *X*2 and *X*1, at 720 and 790 km depth, below the Mariana slab, respectively (Fig. 17). *X*2 at the western edge of the deeply penetrating Mariana slab is possibly the depressed 660-km discontinuity. X1 at the bottom of the high velocity core in the centre of the slab, could either be the phase change from Ringwoodite to perovskite, if the core is cold enough to be still in metastable condition, or possibly more likely, crust in the deformed slab similar to the megalith shown in Ringwood & Irifune (1988).

5 CONCLUSIONS

The large amplitude *X* and also the *SX* phases recorded at the Californian networks, enable us to infer the presence of a reflector located *ca*. 400 km depth *ca*. 550 km west of the present Mariana subduction zone. We interpret this reflector to be a portion of subducted slab that may be the extant remains of the North New Guinea Plate, possibly the bottom side of the oceanic crust. The model of emplacement of the inferred stranded slab is speculative and calls for the slab or its tail to have stayed in the upper mantle at a geodynamically unstable attitude for *ca*. 15 Myr. As shown in numerical experiments by Christensen (1996), even young slabs tend to sink into the lower mantle, and seem to only have long residence times in the upper mantle when they are deposited horizontally atop the 660-km discontinuity. More recent numerical experiments (e.g. Duretz *et al.* 2014) on the other hand show the influx of 3-D effects and of slab age on the complex slab detachment in subduction zones. Possibly a similar scenario holds for the steeply dipping slab segment (or its remnants), we have proposed. The effect of subducting ridges (such as the Ogasawara Plateau and the Caroline ridge, Fig. 2) on subduction history, and the effect of subducting a tectonic suture with a *ca*. 50 Myr step increase in age may also be important in the stability of the stranded slab segment. We suggest that this steeply dipping feature in a backarc basin environment should be accounted for in the models of tectonic evolution of the Mariana margin.

We speculate, following Wright & Muirhead (1969) and Wright (1972), that new evidence for stagnant slabs, and possibly their remnants left behind during subduction, could come from improved array techniques and data from networks like the USArray (http://www.usarray.org/) and the Hi-net (http://www.hinet.bosai.go.jp), combined with new tomographic imaging techniques.

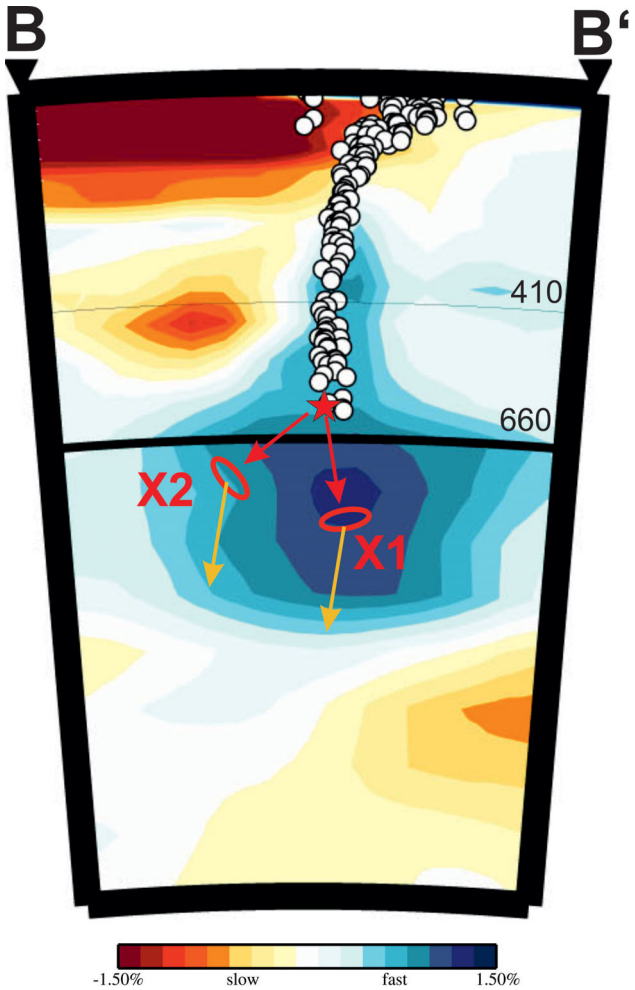

Figure 17. Tomographic cross section through the GAP_P4 model (Obayashi *et al.* 2013) along profile B–B′ from Fig. 2, down to a depth of 1500 km. The 410 (660) discontinuity is indicated by a thin (thick) black line, respectively. The open circles indicate earthquakes from Obayashi *et al.* (2013). The event used by Krüger *et al.* (2001) is given by the red star and the red arrows indicate the ray paths of *P* waves from the source to the scatterers/reflectors, X1 and X1 at 790 and 720 km depth, respectively. The paths from the anomalies to the receiver array (Warramunga array, Australia) are shown with orange arrows, for more details see Krüger *et al.* (2001). The tomographic image is courtesy of M. Obayashi.

ACKNOWLEDGEMENTS

We thank G. Müller (deceased), M. Baumann, H. Paulssen and M. Obayashi for comments to an earlier version of this manuscript. We would also like to thank Ch. Estabrook and an anonymous reviewer, together with the editor G. Laske, for comments that significantly improved the manuscript. We thank D. Suetsugu and S. Tanaka for additional discussions. M. Obayashi kindly provided the tomographic image used in Figs 16 and 17. CW was funded by the Deutsche Forschungsgemeinschaft.

REFERENCES

Bercovici, D. & Karato, I., 2003. Whole-mantle convection and the transition-zone water filter, *Nature,* **425,** 39–44.

Cao, A. & Romanowicz, B., 2007. Locating scatterers in the mantle using array analysis of PKP precursors from an earthquake doublet, *Earth. planet. Sci. Lett.,* **255,** 22–31.

Christensen, U., 1996. The influence of trench migration on slab penetration into the lower mantle, *Earth planet. Sci. Lett.,* **140,** 27–39.

Davies, D., Kelly, E.J. & Filson, J.R., 1971. Vespa process for analysis of seismic signals, *Nature,* **232,** 8–13.

Davis, J.P. & Henson, I.H., 1993. *Xgbm—An X-windows System to Compute Gaussian Beam Synthetic Seismograms,* Teledyne Geotech, Alexandria Lab.

Duretz, T., Gerya, T.V. & Spakmann, W., 2014. Slab detachment in laterally varying subduction zones: 3D numerical modeling, *Geophys. Res. Lett.,* **41,** 1951–1956.

Fukao, Y. & Obayashi, M., 2013. Subducted slabs stagnant above, penetrating through, and trapped below the 660 km discontinuity, *J. geophys. Res.: Solid Earth,* **118,** doi:10.1002/2013JB010466.

Fukao, Y., Kanjo, K. & Nakamura, I., 1978. Deep seismic zone as an upper mantle reflector of body waves, *Nature,* **272,** 606–608.

Fukao, Y., Obayashi, M., Inoue, H. & Nenbai, M., 1992. Subducting slabs stagnant in the mantle transition zone, *J. geophys. Res.,* **97,** 4809–4822.

Grand, S.P., 2002. Mantle shear wave tomography and the fate of subducted slabs, *Phil. Trans. R. Soc. Lond., A,* **360,** 2475–2491.

Grand, S., van der Hilst, R. & Widiyantoro, S., 1997. Global seismic tomography: a snapshot of convection in the Earth, *G.S.A. Today,* **7,** 1–7.

Gubbins, D. & Snieder, R., 1991. Dispersion of P waves in subducted lithosphere: evidence for an eclogite layer, *J. geophys. Res.,* **96,** 6321–6333.

Helffrich, G.R., Stein, S. & Wood, B.J., 1989. Subduction zone thermal structure and mineralogy and their relationship to seismic wave reflections and conversions at the slab/mantle interface, *J. geophys. Res.,* **94,** 753–763.

Hickey-Vargas, R., Hergt, J. & Spadea, P., 1995. *Active Margins and Marginal Basins of the Western Pacific,* pp. 175–197, eds Taylor, B. & Natland, J., Am. Geophys. Union.

Irifune, T. & Ringwood, A.E., 1993. Phase transformations in subducted oceanic crust and buoyancy relationships at depth of 600–800 km in the mantle, *Earth planet. Sci. Lett.,* **117,** 101–110.

Kaneshima, S., 2003. Small-scale heterogeneity at the top of the lower mantle around the Mariana slab, *Earth planet. Sci. Lett.,* **209,** 85–101.

Kaneshima, S. & Helffrich, G.R., 1998. Detection of lower mantle scatterers northeast of the Mariana subduction zone using short-period array data, *J. geophys. Res.,* **103,** 4825–4838.

Kaneshima, S. & Helffrich, G.R., 1999. Dipping low-velocity layer in the mid-lower mantle: evidence for geochemical heterogeneity, *Science,* **283,** 1888–1891.

Kaneshima, S. & Helffrich, G.R., 2003. Sub-parallel dipping heterogeneities in the mid-lower mantle, *J. geophys. Res.,* **108**(B5), 2272, doi:0.1029/2001JB001596.

Kaneshima, S. & Helffrich, G.R., 2009. Lower mantle scattering profiles and fabric below Pacific subduction zones, *Earth planet. Sci. Lett.,* **282,** 234–239.

Kárason, H. & Van der Hilst, R.D., 2000. Constraints on mantle convection from seismic tomography, in *The History and Dynamics of Global Plate Motion,* Vol. 121, pp. 277–288, eds Richards, M.R., Gordon, R. & Van der Hilst, R.D., Geophysical Monograph, American Geophysical Union.

Karato, S., 2011. Water distribution across the mantle transition zone and its implications for global material circulation, *Earth planet. Sci. Lett.,* **301**(3), 413–423.

Kawakatsu, H. & Yoshioka, S., 2011. Metastable olivine wedge and deep dry cold slab beneath southwest Japan, *Earth planet. Sci. Lett.,* **303,** 1–10.

Kennett, B.L.N. & Engdahl, E.R., 1991. Traveltimes for global earthquake location and phase identification, *Geophys. J. Int.,* **105,** 429–465.

Kono, Y., Irifune, T., Ohfuji, H., Higo, Y. & Funakoshi, K., 2012. Sound velocities of MORB and absence of a basaltic layer in the mantle transition region, *Geophys. Res. Lett.,* **39,** L24306, doi:10.1029/2012GL054009.

Krüger, F., Baumann, M., Weber, M. & Scherbaum, F., 2001. Mid-mantle scatterers near the Mariana slab detected with double array technique, *Geophys. Res. Lett.,* **28,** 667–670.

Kustowski, B., Ekström, G. & Dziewoński, A.M., 2008. The shear-wave velocity structure in the upper mantle beneath Eurasia, *Geophys. J. Int.,* **174,** 978–992.

Lee, J., Stern, R.J. & Bloomer, S.H., 1995. Forty million years of magmatic evolution in the Mariana arc: the tephra glass record, *J. geophys. Res.,* **100,** 17 671–17 687.

Li, C., van der Hilst, R.D., Engdahl, E.R. & Burdick, S., 2008. A new global model for P wave speed variations in Earth's mantle, *Geochem. Geophys. Geosyst.,* **9,** Q05018, doi:10.1029/2007GC001806.

Miyamachi, H. *et al.*, , 2009. Construction of the broadband seismic network in Far Eastern Russia for imaging the stagnant slab, *Geophys. Bull. Hokkaido Univ.,* **72,** 37–49 (in Japanese with English abstract).

Muirhead, K.J. & Datt, R., 1976. The Nth root process applied to seismic data, *Geophys. J. R. astr. Soc.,* **47,** 197–210.

Nakanishi, I., 1988. Reflections of P'P' from upper mantle discontinuities beneath the Mid-Atlantic Ridge, *Geophys. J. Int.,* **93,** 335–346.

Nelson, W.R., Snow, J.E., Brandon, A.D. & Ohara, Y., 2013. *Subduction Signature in Backarc Mantle?,* Abstract, Fall AGU meeting, San Francisco, V33A-2718.

Niu, F., Kawakatsu, H. & Fukao, Y., 2003. Seismic evidence for a chemical heterogeneity in the midmantle: a strong and slightly dipping seismic reflector beneath the Mariana subduction zone, *J. geophys. Res.,* **108**(B9), doi:10.1029/2002JB002384.

Obayashi, M., Yoshimitsu, J. & Fukao, Y., 2009. Tearing of stagnant slab, *Science,* **324,** 1173–1175.

Obayashi, M., Yoshimitsu, J., Nolet, G., Fukao, Y., Shiobara, H., Sugioka, H., Miyamachi, H. & Gao, Y., 2013. Finite frequency whole mantle P wave tomography: improvement of subducted slab images, *Geophys. Res. Lett.,* **40,** 1–6.

Panning, M.P., Lekic, V. & Romanowicz, B., 2010. Importance of crustal corrections in the development of a new global model of radial anisotropy, *J. geophys. Res.,* **115,** B12325, doi:10.1029/2010JB007520.

Ringwood, A.E. & Irifune, T., 1988. Nature of the 650-km seismic discontinuity: implications for mantle dynamics and differentiation, *Nature,* **331,** 131–136.

Ritsema, J., van Heijst, H.J., Deuss, A. & Woodhouse, J.H., 2011. S40RTS: a degree-40 shear-velocity model for the mantle from new Rayleigh wave dispersion, teleseismic traveltimes, and normal-mode splitting function measurements, *Geophys. J. Int.,* **184,** doi:10.1111/j.1365-246X.2010.04884.x.

Rost, S., Garnero, E.J. & Williams, Q., 2008. Seismic array detection of subducted oceanic crust in the lower mantle, *J. geophys. Res.,* **113,** doi:10.1029/2007JB005263.

Seno, T., 1984. *Was there a North New Guinea plate?,* Report No. 263, Geol. Surv. of Japan, 29–42.

Seno, T., 1985. *Formation of Active Ocean Margins,* ed. Nasu, N., pp. 469–481, TERRAPUB.

Seno, T. & Maruyama, S., 1984. Paleogeographic reconstruction and origin of the Philippine Sea, *Tectonophysics,* **102,** 53–84.

Shiobara, H., Baba, K., Utada, H. & Fukao, Y., 2009. Ocean bottom array probes stagnant slab beneath the Philippine Sea, *EOS, Trans. Am. geophys. Un.,* **90**(9), 70–71.

Simmons, N.A., Myers, S.C., Johannesson, G. & Matzel, E., 2012. LLNL-G3Dv3: Global P wave tomography model for improved regional and teleseismic travel time prediction, *J. geophys. Res.,* **117,** B10302, doi:10.1029/2012JB009525.

Song, T.A., Helmberger, D.V. & Grand, S.P., 2004. Low-velocity zone atop the 410-km seismic discontinuity in the northwestern United States, *Nature,* **427,** 530–533.

Stern, R.J., 2002. Subduction zones, *Rev. Geophys.,* **40**(4), 1012, doi: 10.1029/2001RG000108.

Vanacore, E, Niu, F.L. & Kawakatsu, H., 2006. Observations of the mid-mantle discontinuity beneath Indonesia from S to P converted waveforms, *Geophys. Res. Lett.,* **33,** doi:10.1029/2005GL025106.

Van der Hilst, R.D. & Seno, T., 1993. Effects of relative plate motion on the deep structure and penetration depth of slabs below the Izu-Bonin and Mariana island arcs, *Earth. planet. Sci. Lett.,* **120,** 395–407.

Van der Hilst, R.D., Engdahl, E.R., Spakman, W. & Nolet, G., 1991. Tomographic imaging of subducted lithosphere below northwest Pacific island arcs, *Nature,* **353,** 37–43.

Van der Hilst, R., Widiyantoro, S. & Engdahl, E.R., 1997. Evidence for deep mantle circulation from global tomography, *Nature,* **386,** 579–584.

Vidale, J.E. & Benz, H., 1992. Upper mantle seismic discontinuities and the thermal structure of subduction zones, *Nature,* **356,** 678–683.

Weber, M., 1988. Computation of body-wave seismograms in absorbing 2-D media using the Gaussian beam method: comparison with exact methods, *Geophys. J.,* **92,** 9–24.

Weber, M. & Wicks, C. Jr., 1996. Reflections from a distant subduction zone, *Geophys. Res. Lett.,* **23,** 1453–1456.

Wessel, P. & Smith, W.H.F., 1991. Free software helps map and display data, *EOS, Trans. Am. geophys. Un.,* **72**(441), 445–446.

Wicks, C. Jr. & Richards, M., 1993. A detailed map of the 660–kilometer discontinuity beneath the Izu-Bonin subduction zone, *Science,* **261,** 1424–1427.

Wicks, C. Jr. & Weber, M., 1996. Seismic evidence for a fossil subduction zone beneath the Philippine Plate, *Ann. Geophys.,* **14**(Suppl. I), C45.

Wicks, C. Jr., Weber, M., Breger, L., LeStunff, Y. & Romanowicz, B., 1995. A broadband investigation of the lithosphere-mantle join near the Marianas trench, *EOS, Trans. Am. geophys. Un.,* **46,** F401.

Wicks, C., Weber, M., Le Stunff, Y. & Romanowicz, R., 1996. California broadband array evidence for an upper mantle reflector beneath the West Mariana Ridge [abstract], Fall AGU meeting, San Francisco, *EOS, Trans. Am. geophys. Un.,* **77**(46, Suppl.), F492.

Wicks, C.W., Weber, M., Le Stunff, Y. & Romanowicz, R., 1997. Seismic evidence for a steeply dipping reflector in the mantle transition zone [abstract], in *Proceedings of the 9th European Geological Union,* Strasbourg, France.

Wright, C., 1972. Array studies of seismic waves arriving between P and PP in the distance range 90 deg to 115 deg, *Bull. seism. Soc. Am.,* **62**(1), 385–400.

Wright, C. & Muirhead, K.J., 1969. Longitudal waves from the Novaya Zemlya nuclear explosion of October 27, 1966, recorded at the Warramunga Seismic Array, *J. geophys. Res.,* **74**(8), 2034–2048.